Article

3D N-heterocyclic covalent organic frameworks for urea photosynthesis from NH_3 and CO_2

Ning Li [1], Jiale Zhang[1], Xiangdong Xie[2], Kang Wang [1]✉, Dongdong Qi [1]✉, Jiang Liu [2], Ya-Qian Lan [2] & Jianzhuang Jiang [1]✉

Artificial photosynthesis of urea from NH_3 and CO_2 seems to remain still essentially unexplored. Herein, three isomorphic three-dimensional covalent organic frameworks with twofold interpenetrated ffc topology are functionalized by benzene, pyrazine, and tetrazine active moieties, respectively. A series of experiment results disclose the gradually enhanced conductivity, light-harvesting capacity, photogenerated carrier separation efficiency, and co-adsorption capacity towards NH_3 and CO_2 in the order of benzene-, pyrazine-, and tetrazine-containing framework. This in turn endows tetrazine-containing framework with superior photocatalytic activity towards urea production from NH_3 and CO_2 with the yield of 523 μmol g^{-1} h^{-1}, 40 and 4 times higher than that for benzene- and pyrazine-containing framework, respectively, indicating the heterocyclic N microenvironment-dependent catalytic performance for these three photocatalysts. This is further confirmed by in-situ spectroscopic characterization and density functional theory calculations. This work lays a way towards sustainable photosynthesis of urea.

Urea serves as the most critical nitrogen fertilizer to meet the needs of a growing population[1–4]. Currently, industrial urea production is still dependent on the Bosch-Meiser two-step synthesis reaction consuming NH_3 and CO_2 under high temperature and pressure[5–9]. This complicated urea production process is energy-intensive, consuming *ca.* 30 billion kJ of energy and emitting *ca.* 2 tons of CO_2 for every ton of urea[10]. As a result, adapting the core synthesis chemical reactions to achieve efficient urea production under mild conditions with less energy requirement and environmentally friendliness becomes a promising alternative to conventional ones[11]. Photo-catalytic technologies driven by solar energy are expected to show great potential for energy-saving production of zero-carbon urea via CO_2 coupled with nitrogenous substances[12,13]. Quite recently, few studies have been reported on urea photosynthesis with N_2 and CO_2 as starting material and H_2O as a hydrogen source catalyzed by

inorganic nano-catalysts[14–18]. In 2022, Zhang and colleagues carried out the photosynthesis of urea with a rate of 7.2 μmol g^{-1} h^{-1} through the photocatalytic reduction of CO_2 and N_2 by Cu SA-TiO_2[14]. In 2023, urea photosynthesis was achieved from N_2 and CO_2 with yields of 6.4 and 9.2 μmol g^{-1} h^{-1} depending on CeO_2-Vo and Pd–CeO_2, respectively[15,16]. In the following 2024, urea production was show-cased at a rate of 24.95 μmol g^{-1} h^{-1} under the photocatalysis of Ru particles on TiO_2 with N_2/NO_3^- and CO_2 as starting materials[17]. This was followed by the photo-production of urea from CO_2 and N_2 with a rate of 78 μmol h^{-1} L^{-1} catalyzed by Ni_1-CdS/WO_3 in the same year[18]. However, the photocatalytic performance is unsatisfactory in terms of both the low urea production rate and in particular poor selectivity as clearly revealed in these reports. Moreover, these inorganic nano-catalysts employed also suffer from not well-defined chemical composition and structure/electronic structure, making it hard to

[1]Beijing Key Laboratory for Science and Application of Functional Molecular and Crystalline Materials, Department of Chemistry and Chemical Engineering, School of Chemistry and Biological Engineering, University of Science and Technology Beijing, Beijing, China. [2]Guangdong Provincial Key Laboratory of Carbon Dioxide Resource Utilization, School of Chemistry, South China Normal University, Guangzhou, China. ✉e-mail: kangwang@ustb.edu.cn; qdd@ustb.edu.cn; jianzhuang@ustb.edu.cn

1

effectively clarify the structure-activity relationship towards further improving the photocatalytic performance.

Nevertheless, it is worth noting that urea synthesis from N_2 and CO_2 starting materials and H_2O as hydrogen sources under either thermal, electrochemical, or photochemical catalysis has to face the very high activation energy of 945 kJ mol^{-1} for the triple N≡N bond and the very high reaction enthalpy change ($\Delta_r H_m^{\ominus}$) of 1264 kJ mol^{-1} for

$$2N_2 + 2CO_2 + 4H_2O = 2CO(NH_2)_2 + 3O_2 \qquad (1)$$
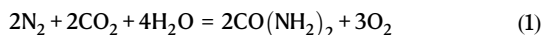
In contrast, with the employment of NH_3 and CO_2 as starting materials based on the present industrial urea production route, the C-N coupling reaction for the urea generation would become a thermodynamically spontaneous one with a negative $\Delta_r H_m^{\ominus}$ of −135.5 kJ mol^{-1} for[19–21]

$$2NH_3 + CO_2 = CO(NH_2)_2 + H_2O \qquad (2)$$
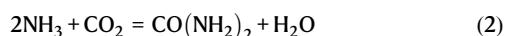
Furthermore, compared with the stable N≡N bond in N_2, the lone pair electrons in NH_3 are naturally reactive centers, in favor of fast reaction dynamics. As a total result, photosynthesis of urea from NH_3 and CO_2 appears more promising for future practical industrial applications. This, however, seems to remain still essentially unexplored, limited to the very late trial over Pd@TiO$_2$/Gr catalyzed urea photosynthesis with a series of nitrogenous sources including NO_3^-, N_2, and NH_3 as the sole report[22], to the best of our knowledge.

Covalent organic frameworks (COFs) represent a new class of porous materials constructed from molecular building blocks linked via covalent bonds, which have shown great application potential in gas storage and separation[23], energy storage[24], optoelectronic devices[25], and catalysis owing to their advantages of low density, excellent stability, and high porosity[26–30]. In particular, their advantageous light absorption and emission characteristics, exceptional crystallinity, structural multiplicity, and stability render COFs an alluring option for potential applications in the domain of photocatalysis[31,32]. Furthermore, COFs can be meticulously modulated to create specific reaction sites and band structures through the rational design of the molecular building blocks, offering a convincing platform to verify the intrinsic mechanism and in turn achieve the desired photocatalytic performance. Recently, the incorporation of nitrogen (N)-heterocycles into COFs has been demonstrated to be a promising strategy to promote various unimolecular reactions including oxygen reduction reaction and CO_2 reduction reaction, due to the exemplary optical and electrical properties of N-heterocycles ascribed to their conjugated π-systems and excellent electron affinity[33,34]. Particularly, the microenvironment of catalytic reaction can be adjusted by changing the number and position of N atoms in the N-heterocycles of COFs, favoring to optimization of photocatalytic performance towards coupling reaction. In particular, N-heterocycles with directly connected N atoms such as tetrazine rings are supposed to be able to synergistically activate nitrogen and carbon sources to promote the formation of C−N coupling products.

Herein, three isomorphic three-dimensional (3D) COFs with two-fold interpenetrated ffc topology (namely 3D-TPT-COF, 3D-PDDP-COF, and 3D-TBBD-COF) were functionalized by benzene, pyrazine, and tetrazine active cores, respectively, to modulate the catalytic microenvironment through the change in the number of heterocyclic N atoms on the active cores. Electric conductivity measurement, UV-vis diffuse reflectance spectra, Nyquist plots, and transient photocurrent spectroscopic results unveil the superior semiconductivity, light absorption, and photogenerated carrier separation efficiency of 3D-TBBD-COF compared to 3D-TPT-COF and 3D-PDDP-COF owing to the N-rich nature of the tetrazine moieties in 3D-TBBD-COF. Moreover, gas adsorption experiments reveal the higher adsorption capacity of 3D-TBBD-COF to both NH_3 (131 cm^{3}g^{-1}) and CO_2 (33 cm^{3}g^{-1}) at room

temperature compared to 3D-TPT-COF (86 and 24 cm^{3}g^{-1}) and 3D-PDDP-COF (101 and 30 cm^{3}g^{-1}) owing to the more exposed lone pair electrons in the tetrazine-containing framework of 3D-TBBD-COF over the benzene-containing 3D-TPT-COF and pyridine-containing 3D-PDDP-COF. The geometrical and electronic structural advantages endow 3D-TBBD-COF with superior photocatalytic activity towards urea production from CO_2 and NH_3 with the yield of 523 μmol g^{-1} h^{-1}, 40 and 4 times higher than that for 3D-TPT-COF and 3D-PDDP-COF, respectively, indicating the heterocyclic N microenvironment-dependent catalytic performance for these COFs photocatalysts. In addition, a series of in-situ spectroscopic characterization and density functional theory calculations demonstrate the effective synergistic co-adsorption and co-activation of NH_3 and CO_2 by the two directly connected N atoms of the tetrazine moieties in 3D-TBBD-COF due to the formation of N=N unit-based cycled intermediate depending on hydrogen bonding interaction between NH_4^+ and CO_2 dissolved in water, promoting the C-N coupling reaction to form the crucial intermediate *NH$_2$C$^+$O and in turn the photocatalytic production of urea. This work lays a way towards sustainable photosynthesis of urea.

Results and discussion

As shown in Fig. 1a and Supplementary Figs. 1–5, the solvothermal reaction of 1,3,5-tris(p-formylphenyl)benzene (TFPB) with 1,1':4',1"-terphenyl-3,3",5,5"-tetraamine (TPT), 1,3,5-tris(4-aminophenyl)benzene (TAPB) with 5,5'-(pyrazine-2,5-diyl)diisophthalaldehyde (PDDP), and TFPB with 5,5'-(1,2,4,5-tetrazine-3,6-diyl)bis-benzene-1,3-diamine (TBBD) under the same condition generates 3D-TPT-COF, 3D-PDDP-COF, and 3D-TBBD-COF, respectively. It is worth noting that the three COFs are constructed from square-planar and trigonal-planar building units via a [4 + 3] condensation reaction, which can generate high symmetry 3D COFs with relatively high pore volume and interconnected nanochannels, favoring the exposure of the active sites and mass transfer[35]. The Fourier transform infrared (FT-IR) spectra of these three COFs show a strong C=N stretching vibration band at 1693 cm^{-1}, Fig. 1b. This, together with the disappearance of the C=O bond at 1724 cm^{-1} and the N-H bond at 3330 cm^{-1}, indicates the successful condensation between the amine and aldehyde precursors[36,37]. In addition, the characteristic C signal of the imine bond is observed at 151 ppm in the ^{13}C solid-state nuclear magnetic resonance (^{13}C ssNMR) spectra of the three COFs, confirming the formation of imine bonds in these COFs, Fig. 1c and Supplementary Figs. 6 and 7. Nitrogen adsorption/desorption isotherms of these COFs were obtained at 77 K to investigate their pore structure, Fig. 1d. Based on the Brunauer−Emmett−Teller (BET) model, the specific surface areas of 3D-TPT-COF, 3D-PDDP-COF, and 3D-TBBD-COF amount to 602, 461, and 556 cm^{3}g^{-1}, respectively, with the pore size calculated to center at 10.5, 11.1, and 11.3 Å according to the nonlocal density functional theory (NLDFT), Supplementary Fig. 8, revealing their micropore nature. It is worth noting that the inclination of isotherms with open hysteresis loops in the P/P$_0$ range of 0.2-1.0 suggests the presence of narrow and rigid slit pores between the COFs particles. Thermogravimetric analysis (TGA) discloses a decomposition temperature of *ca.* 400 °C for the three COFs, proving their high thermal stability, Supplementary Figs. 9–11. In particular, the PXRD patterns of these three COFs remain almost unchanged after being dispersed in solvents including H_2O, acetonitrile, ethanol, and ammonia for 7 days, Supplementary Figs. 12–14, further confirming their high stability.

The crystalline structures of 3D-TPT-COF, 3D-PDDP-COF, and 3D-TBBD-COF were determined by PXRD measurement and simulation calculation. All three COFs show a series of diffraction peaks in their PXRD patterns, Fig. 1e−g, demonstrating their good crystalline nature. As shown in Supplementary Figs. 15−24, to determine their lattice packing, 8 possible nets including 3D pto, tbo, mhq-z, fjh, gee, ffc, and 2D bex and tth topologies were constructed and optimized[35,38–40]. As can be found, the experimentally revealed PXRD pattern of 3D-TBBD-
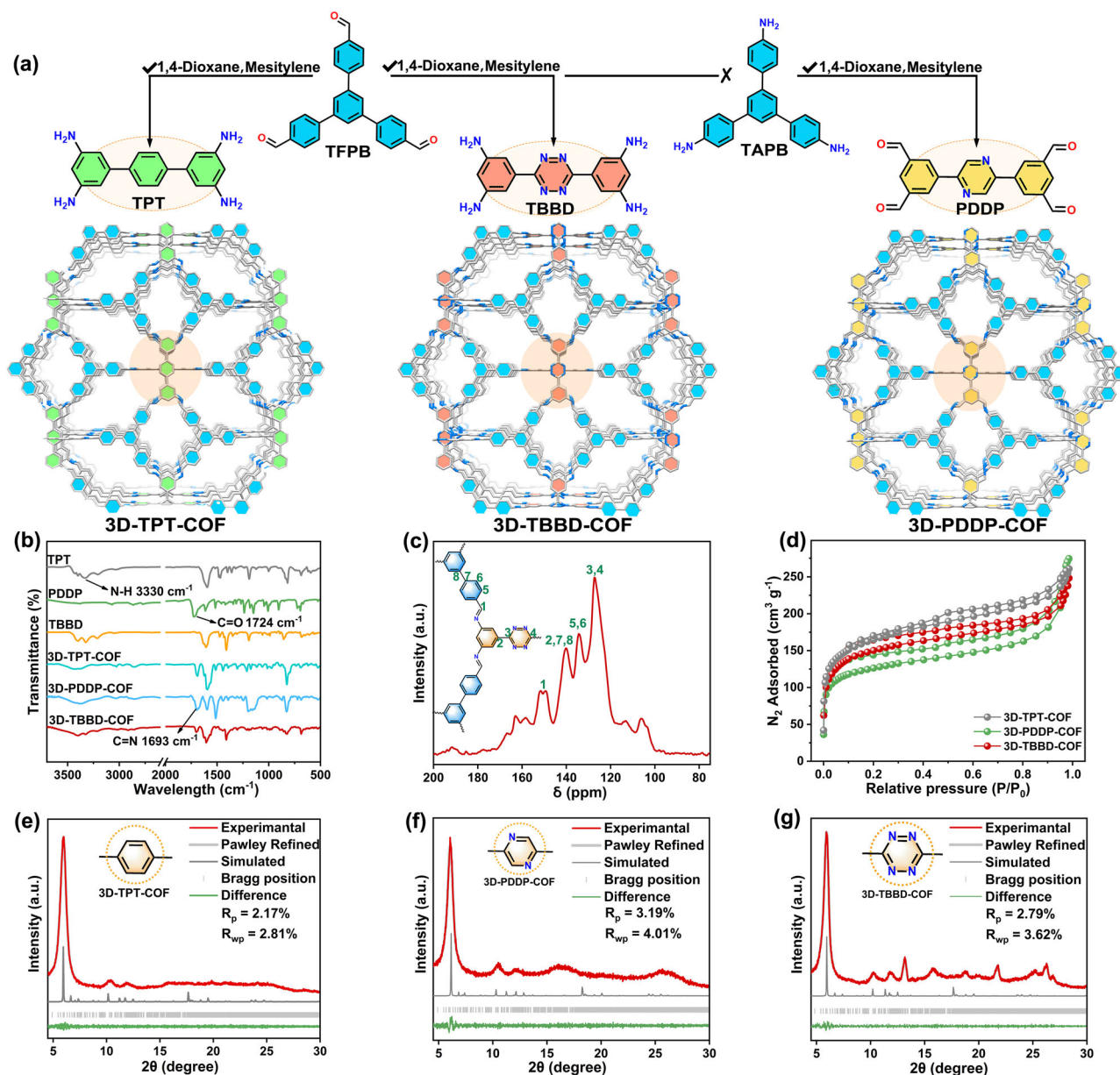
Fig. 1 | Structural schematic and characterization of COFs. a Schematic synthesis and (**b**) FT-IR spectra of 3D-TPT-COF, 3D-PDDP-COF, and 3D-TBBD-COF. **c** ^{13}C ssNMR spectrum of 3D-TBBD-COF. **d** N_2 sorption isotherms of 3D-TPT-COF (gray), 3D-PDDP-COF (green), and 3D-TBBD-COF (red). PXRD patterns of (**e**) 3D-TPT-COF, **f** 3D-PDDP-COF, and (**g**) 3D-TBBD-COF.

COF matches well with the simulated one of the twofold interpenetrated ffc topology with the best agreement factors of $R_p = 2.79\%$ and $R_{wp} = 3.62\%$ according to the Pawley refinement, Fig. 1a–g. The unit cell parameters of 3D-TBBD-COF are yielded as $a = 82.09$ Å, $b = 24.66$ Å, $c = 14.58$ Å, $\alpha = \beta = \gamma = 90°$ in the Pm space group. According to the Pawley refinement, 3D-PDDP-COF and 3D-TPT-COF are isomorphic to 3D-TBBD-COF and also adopt the twofold interpenetrated ffc topology. The diffraction peaks of 3D-TBBD-COF at 5.9, 10.2, 11.9, 13.2, 18.7, and 25.1° are attributed to the (101), (421), (430), (402), (103), and (204) facets, respectively. The unit cell parameters of 3D-PDDP-COF are determined to be $a = 83.34$ Å, $b = 23.61$ Å, $c = 14.59$ Å, $\alpha = \beta = \gamma = 90°$ in the Pm space group with the observed diffraction peaks at 6.0, 10.4, 13.3, and 25.7° assigned to the (101), (421), (402), and (204) Bragg peaks, Fig. 1f. As for 3D-TPT-COF, the diffraction peaks at 5.9, 10.3, and 12.0° can be attributed to the (101), (421), and (402) facets of a lattice in the Pm space group with cell parameters of $a = 83.70$ Å,

$b = 23.47$ Å, $c = 15.08$ Å, $\alpha = \beta = \gamma = 90°$, Fig. 1e. The scanning electron microscope (SEM), transmission electron microscope (TEM), and energy dispersive spectroscopy (EDS) were used to analyze the morphology and elemental distribution of these three 3D COFs. SEM and TEM images disclose their irregular spherical shapes with a size of *ca.* 300-500 nm, Supplementary Fig. 25. High-resolution TEM (HR-TEM) images exhibit distinct lattice stripes of 3D-TPT-COF, 3D-PDDP-COF, and 3D-TBBD-COF with a spacing of 0.98, 1.09, and 1.11 nm, respectively, Supplementary Fig. 26, corresponding to their (101) Bragg peaks, further proving their good crystalline nature. In addition, EDS mapping images reveal the uniformly distributed C and N over the COFs samples, Supplementary Fig. 27.

The semiconductivity property, light-harvesting capacity, and electronic structure of the series of three COFs were investigated by electric conductivity measurement, UV-vis diffuse reflectance spectra (UV-vis-DRS), and Mott-Schottky curves. As shown in Fig. 2a, along with
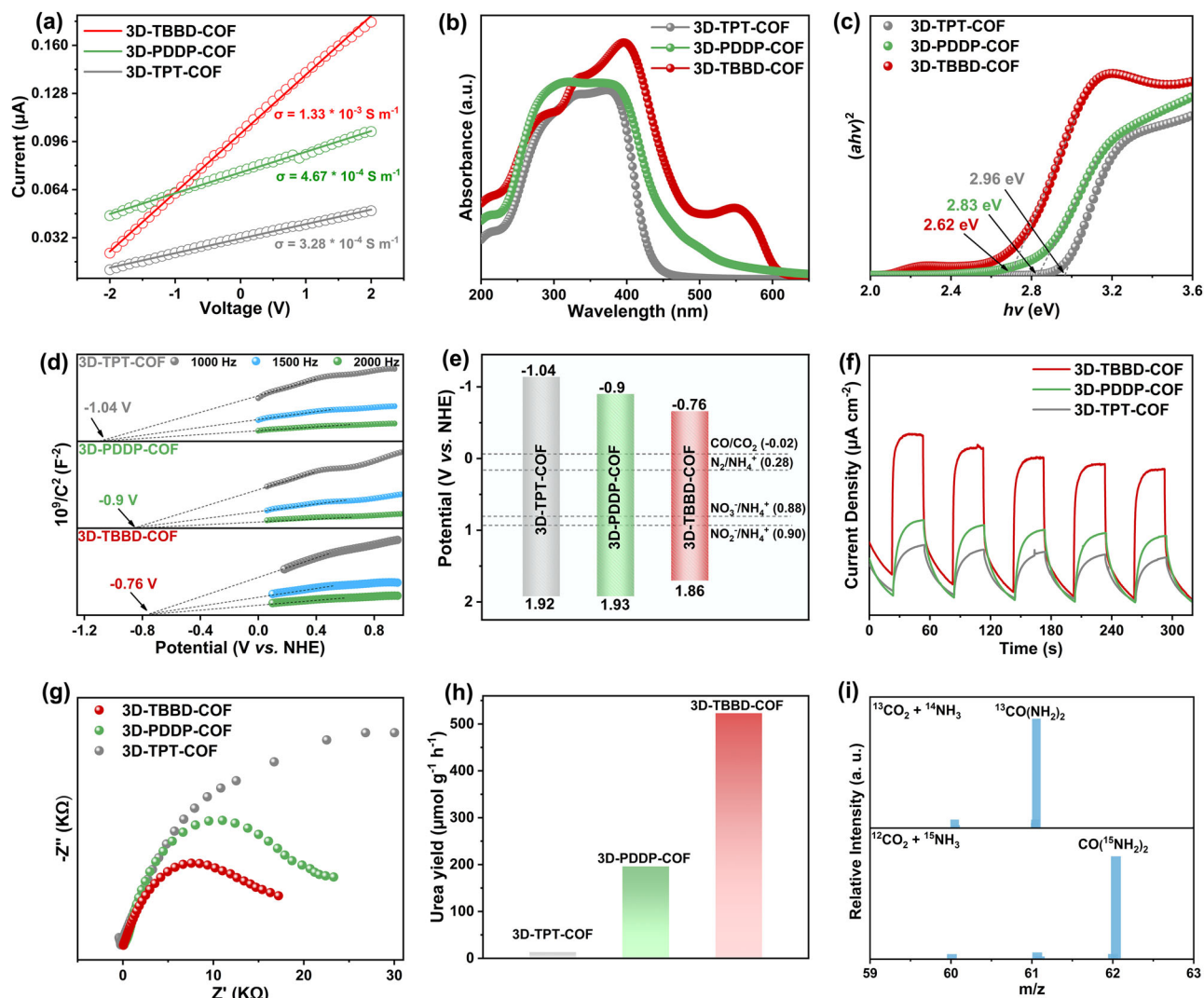
Fig. 2 | Characterization of COFs and urea photoproduction. a Current-voltage (**b**) UV-vis DRS, **c** Tauc plots, **d** Mott–Schottky plots, **e** energy band structure, **f** transient photocurrent spectra, and (**g**) Nyquist plots of 3D-TPT-COF (gray), 3D-PDDP-COF (green), and 3D-TBBD-COF (red). **h** Urea formation rate using 3D-TPT-COF, 3D-PDDP-COF, and 3D-TBBD-COF as photocatalyst. **i** HR-MS spectra of 3D-TBBD-COF photocatalytic $^{13}CO_2 + {}^{14}NH_3$ and $^{12}CO_2 + {}^{15}NH_3$ synthesis systems.

the replacement of the benzene moiety in 3D-TPT-COF by pyrazine moiety in 3D-PDDP-COF and tetrazine moiety in 3D-TBBD-COF, the electric conductivity gets increased from 3.28×10^{-4} to 4.67×10^{-4} and 1.33×10^{-3} S m^{-1} in the same order due to the electron-withdrawing inductive effect of heterocyclic N atoms[41], confirming their semiconductive nature. Also due to the same reason, the electronic absorption range increases from 200-440 to 200-500 and 200-600 nm for 3D-TPT-COF, 3D-PDDP-COF, and 3D-TBBD-COF, respectively, Fig. 2b, indicating the improved light harvesting capacity along with the increase in the number of heterocyclic N atoms in the framework. Additionally, the bandgap widths of 3D-TPT-COF, 3D-PDDP-COF, and 3D-TBBD-COF are calculated to be 2.96, 2.83, and 2.58 eV, respectively, according to Tauc plots, Fig. 2c, revealing the narrowest band gap of 3D-TBBD-COF, which can help facilitate the transfer of photogenerated charges. Mott-Schottky measurements show a flat band of -1.04, -0.90, and -0.76 V $vs.$ normal hydrogen electrode (NHE) for 3D-TPT-COF, 3D-PDDP-COF, and 3D-TBBD-COF, respectively, Fig. 2d. As a result, the valence band (VB) is calculated to be 1.92, 1.93, and 1.86 V $vs.$ NHE for 3D-TPT-COF, 3D-PDDP-COF and 3D-TBBD-COF. Obviously, the CBs of these three COFs are more negative than the potential of CO_2/CO, while their VBs are more positive than the potentials of N_2/NH_4^+, NO_2^-/NH_4^+, and NO_3^-/NH_4^+, implying the

capacity of the three COFs to simultaneously catalyze CO_2 reduction reaction and NH_3 oxidation reaction, Fig. 2e. As shown in Fig. 2f, 3D-TBBD-COF displays higher photocurrent response signals than those for 3D-TPT-COF and 3D-PDDP-COF, indicating its enhanced photogenerated electron-hole separation efficiency owing to the introduction of tetrazine moiety into the framework. Nevertheless, 3D-TBBD-COF exhibits a smaller semicircle diameter in the Nyquist curve in comparison with 3D-TPT-COF and 3D-PDDP-COF, Fig. 2g, revealing the smallest charge transfer resistance of 3D-TBBD-COF among the three COFs. These results indicated that the photocurrent response and charge transfer characteristics of the three COFs were gradually improved along with the increase in the number of N atoms in the framework due to the enhanced electron-absorbing inductive effect of heterocyclic N atoms, in favor of improving the photocatalytic performance.

The photocatalytic performance of all the prepared COFs towards the urea production from NH_3 and CO_2 was tested in a batch reactor under the irradiation of a 300 W xenon lamp. Photocatalytic tests were performed in pure water by adding NH_3 and CO_2 (2:1, v/v) as feedstock and the prepared COFs as the catalysts. As shown in Fig. 2h and Supplementary Fig. 28, 3D-TPT-COF without N-containing heterocycles in the framework displays a very small urea production rate

of 13 $\mu mol\ g^{-1}\ h^{-1}$, revealing its negligible photocatalytic activity towards urea production from NH_3 and CO_2. Replacing the benzene moieties in 3D-TPT-COF with the pyrazine moieties in 3D-PDDP-COF leads to a significantly increased urea production rate of 196 $\mu mol\ g^{-1}\ h^{-1}$ for 3D-PDDP-COF, suggesting the effect of N-containing heterocycles in the framework on promoting the formation of urea from NH_3 and CO_2 coupling. Further increase in the N atomic number via replacing the pyrazine moiety in 3D-PDDP-COF with tetrazine moiety in 3D-TBBD-COF results in a further significantly increased urea production rate of 523 $\mu mol\ g^{-1}\ h^{-1}$ for the latter material, confirming the active center nature of N atoms in the N-containing heterocycles of the frameworks towards urea production. In particular, the four times higher urea production rate of 3D-TBBD-COF in comparison with 3D-PDDP-COF also implies the synergistic effect of the two directly connected N active sites in a pair of $N = N$ units of tetrazine moieties on achieving C-N coupling for the formation of urea from NH_3 and CO_2. Furthermore, the apparent quantum yield (AQY) of 3D-TBBD-COF was measured at different wavelengths with a maximum value of 0.32% observed at 420 nm, Supplementary Fig. 29. Impressively, the urea yield of 3D-TBBD-COF remains almost constant after five consecutive cycles of the reaction, Supplementary Fig. 30, revealing the excellent photostability of 3D-TBBD-COF. In addition, the recycled 3D-TBBD-COF sample after photocatalytic cycles exhibits a very similar PXRD pattern, XPS spectrum, and FT-IR spectrum to those for the 3D-TBBD-COF sample before photocatalytic cycles, Supplementary Figs. 31–33, further confirming its excellent stability during photocatalytic reaction process. At the end of this section, it is noteworthy that both conventional industrial production and electrochemical production can form ca. 1.4-2.0 tons of CO_2 per ton of urea. In contrast, utilizing the present photocatalytic process, carbon dioxide acts as a continuously consuming feedstock. In addition, the costs of energy and feedstock input for the photocatalytic urea production were also calculated based on the life cycle cost approach. According to the calculation result, photocatalytic urea production in the present case offers lower cost, USD 70/ton urea, than conventional industrial urea production, USD 410/ton urea as well as electrochemical urea production, USD 360/ton urea. With an annual production of 21 million tons of urea, this photocatalytic urea production can save 6 billion USD, in detail for the data sources see Supplementary note[10,42,43].

To identify the role of 3D-TBBD-COF in the photocatalytic system, various control experiments were carried out, Supplementary Figs. 34 and 35. In the absence of COF photocatalysts, no urea was generated in the reactor, manifesting the photocatalyst nature of 3D-TBBD-COF in photocatalytic NH_3 and CO_2 coupling reaction to produce urea. As expected, the urea production reaction carried out in the dark gives no target product, disclosing the light irradiation promotion nature for the urea production from NH_3 and CO_2. Nevertheless, no urea was detected without adding NH_3 or CO_2 into the reactor, revealing the origination of the urea from the coupling reaction between CO_2 and NH_3. To confirm the nitrogen and carbon sources of urea generated, photocatalytic experiments were performed with $^{15}NH_3$ and $^{13}CO_2$ as the feedstock, respectively. As displayed in Fig. 2i and Supplementary Fig. 36, the employment of $^{15}NH_3$ and $^{13}CO_2$ as the reactant leads to the observation of a signal at $m/z = 62$ and 61, respectively, in the high-resolution mass (HR-MS) spectra, corresponding to the ^{15}N and ^{13}C labeled urea molecules, confirming the urea origination from NH_3 and CO_2 coupling reaction.

In-situ diffuse reflectance infrared fourier transform (DRIFT) spectroscopy was further performed to trace the adsorption process of CO_2 and NH_3 on the COFs, Fig. 3a–c and Supplementary Figs. 37 and 38. As shown in Fig. 3a, b, in the in-situ DRIFT spectra of 3D-TBBD-COF for CO_2 adsorption in water, the peaks at 1668, 1542, and 1350 cm^{-1} due to the $C = O$, COO^-, and HCO_3^- stretching bands of the adsorbed CO_2 molecules appeared and increased along with the

increase of adsorption time[44,45], while new two bands get appeared at 1360, and 1030 cm^{-1} due to the N-H stretching and bending vibration of the adsorbed NH_3 in the in-situ DRIFT spectra of 3D-TBBD-COF for NH_3 adsorption in water[46,47]. These results prove the CO_2 and NH_3 adsorption capacity of 3D-TBBD-COF. In particular, the $C = O$ and COO^- vibration band at 1600, and 1517 cm^{-1} and N-H vibration band at 1363 and 1029 cm^{-1} are more significantly observed in the in-situ DRIFT spectra of 3D-TBBD-COF for CO_2 and NH_3 co-adsorption compared to those for sole CO_2 or NH_3 adsorption, Fig. 3c, revealing synergistic adsorption of 3D-TBBD-COF for CO_2 and NH_3 owing to the spatial confinement effect induced by the tetrazine moieties as detailed below[48–50]. In comparison, 3D-TPT-COF exhibit obviously weaker bands at 1665 and 1050 cm^{-1} than 3D-TBBD-COF and 3D-PDDP-COF during the absorption processes of CO_2 and NH_3, Supplementary Figs. 37 and 38, revealing the weakened adsorption capacity of 3D-TPT-COF for CO_2 and NH_3. This in turn leads to their inferior photocatalytic performance towards NH_3 and CO_2 coupling to produce urea.

The NH_3/CO_2 adsorption isotherm measurements were carried out at room temperature by static volumetric method to investigate the adsorption activity of the prepared three COFs towards the reaction substrates. As shown in Supplementary Figs. 39–42, the NH_3 and CO_2 uptakes of 3D-TPT-COF at $P/P_0 = 1.0$ under room temperature amount to 86 and 24 $cm^3 g^{-1}$, respectively. As the increase in the number of heterocyclic N atoms in the framework, the NH_3/CO_2 adsorption capacity of 3D-PDDP-COF and 3D-TBBD-COF increased to 101/30 and 131/33 $cm^3 g^{-1}$ at $P/P_0 = 1.0$ and 298 K, respectively. Due to their same twofold interpenetrated ffc topology and very close specific surface area, these results indicate the effect of the heterocyclic N atoms on enhancing the NH_3 and CO_2 adsorption capacity, which in turn can promote the photocatalytic NH_3 and CO_2 coupling reaction to generate urea.

To clarify the adsorption mechanism for the CO_2 and NH_3 on the COFs, adsorption energy calculations were performed at the level of M06-2X/6-311 G(d). As shown in Fig. 3d, e, once NH_3 is dissolved into water, its main existing form will immediately change to NH_4^+ ion. It is worth noting that as a typical electron-deficient moiety, tetrazine (Tz) moiety with two $N = N$ units in 3D-TBBD-COF would certainly receive electrons from the adjacent benzene moieties. This results in a negative-charged active center on the Tz moiety, endowing Tz moiety with the adsorption capacity for CO_2 (also dissolved in water) and NH_4^+ with an adsorption energy of −85 and −13 $kJ\ mol^{-1}$, respectively, due to the mutual attraction of positive/negative charged centers. In particular, the very short N...N distance of ~1.4 Å in the $N = N$ unit of tetrazine moiety allows the formation of a co-adsorbing structure of heptatomic ring with an increased adsorption energy of ~136 $kJ\ mol^{-1}$ due to the formation of $O = C = O...H-NH_3^+$ hydrogen bonding, favoring the C-N coupling from CO_2 and NH_3, Fig. 3e. In contrast, due to the lack of two directly connected N atoms, the same co-adsorbing and co-activation structure cannot be formed in either 3D-PDDP-COF or 3D-TPT-COF, Fig. 3d, e and Supplementary Figs. 43 and 44.

The catalytic conversion process of CO_2 and NH_3 on the COFs was also monitored by in-situ DRIFT spectroscopy, Fig. 3f–h. As expected, new absorption bands appeared at 1702, and 1405 cm^{-1} in the in-situ DRIFT spectra of the 3D-TBBD-COF photocatalytic system, corresponding to the antisymmetrical $*NH_2C^+O$ stretching vibration of urea and the C-N stretching vibration of both urea and reaction intermediates[51], respectively, Fig. 3h. Their intensity steadily grows along with the reaction time, disclosing the successful C-N coupling and the production of urea from NH_3 and CO_2 under the photocatalysis of 3D-TBBD-COF. In addition, the intensity for the band at 1052 cm^{-1} due to adsorbed NH_3 gets significantly decreased due to the consumption of adsorbed NH_3 after C−N coupling. In comparison, the in-situ DRIFT spectra of the 3D-PDDP-COF photocatalytic system display very weak bands at 1401 cm^{-1} even after photoreaction for 180 s,
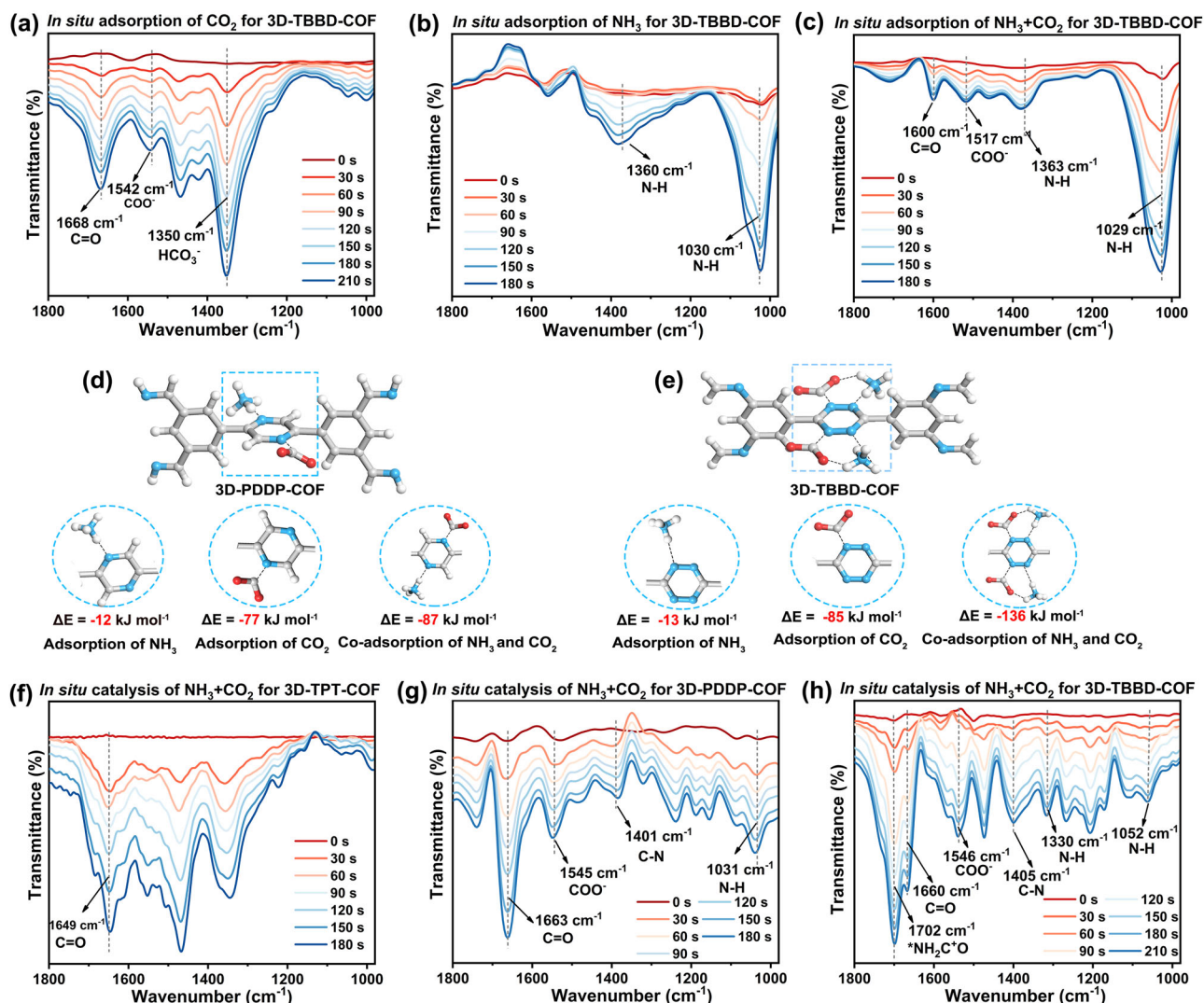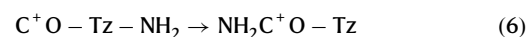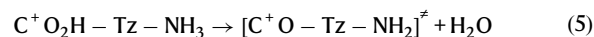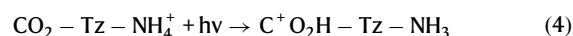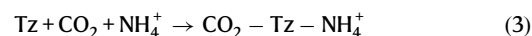
Fig. 3 | In situ DRIFT spectra and adsorption structure of COFs. In-situ DRIFT spectra of 3D-TBBD-COF for (**a**) CO_2, **b** NH_3, and (**c**) $CO_2 + NH_3$ adsorption at different times, respectively. Adsorption structures and adsorption energies for CO_2, NH_3, and $CO_2 + NH_3$ on (**d**) 3D-PDDP-COF and (**e**) 3D-TBBD-COF (C: gray; N: blue; O: red; H: white). In-situ DRIFT spectra of (**f**) 3D-TPT-COF, **g** 3D-PDDP-COF, and (**h**) 3D-TBBD-COF photocoupling CO_2 and NH_3 for urea production at different times.

Fig. 3g, manifesting the lower activity of 3D-PDDP-COF for C–N coupling from CO_2 and NH_3. Moreover, the absorption bands due to the C–N and antisymmetric $*NH_2C^+O$ stretching vibrations are not observed in the in-situ DRIFT spectra of the 3D-TPT-COF photocatalytic system, Fig. 3f, indicating its incapability of photocatalytic C–N coupling from CO_2 and NH_3 owing to the lack of N-containing aromatic moiety, in line with other experimental findings as mentioned above. 3D-TBBD-COF exhibits significantly enhanced CO_2 and NH_3 co-adsorption and co-activation performance due to the existence of $N = N$ units in the tetrazine moiety of 3D-TBBD-COF. Obviously, the regulation of the microenvironment by changing the number of N atoms in the active core can effectively improve the adsorption and catalysis of COFs towards the reaction substrates.

To clarify the photocatalytic mechanism for the urea generation from CO_2 and NH_3 on the COFs, the Gibbs free energy calculations were carried out at the level of M06-2X/6-311 G(d). Based on the calculation results, the full catalytic route on 3D-TBBD-COF could be divided into three stages: (1) Photon capture and generation of excited tetrazine moiety (Tz*); (2) the first C–N coupling process with the help of electron-withdrawing inductive effect of two directly connected N atoms in the $N = N$ units of Tz moiety; (3) the second C–N coupling

process owing to the spatial confinement effect induced by the Tz moiety. As can be seen in Fig. 4a, b, once the photosensitizer Tz captures a photon with a wavelength in the range of 200-600 nm, the reaction will start from the hydrogen transfer from NH_4^+ to CO_2 along the heptatomic ring according to Eqs. (3) and (4) with an energy barrier of 1.31 eV. The next step involves the dehydration process to produce two unstable intermediate species $*C^+O$ and $*NH_2$ with an unpaired electron according to Eq. (5). In the next moment, $*C^+O$ and $*NH_2$ will quickly combine into the half urea NH_2C^+O according to Eq. (6), completing the first C–N coupling process.

$$Tz + CO_2 + NH_4^+ \rightarrow CO_2 - Tz - NH_4^+ \quad (3)$$

$$CO_2 - Tz - NH_4^+ + hv \rightarrow C^+O_2H - Tz - NH_3 \quad (4)$$

$$C^+O_2H - Tz - NH_3 \rightarrow [C^+O - Tz - NH_2]^{\neq} + H_2O \quad (5)$$
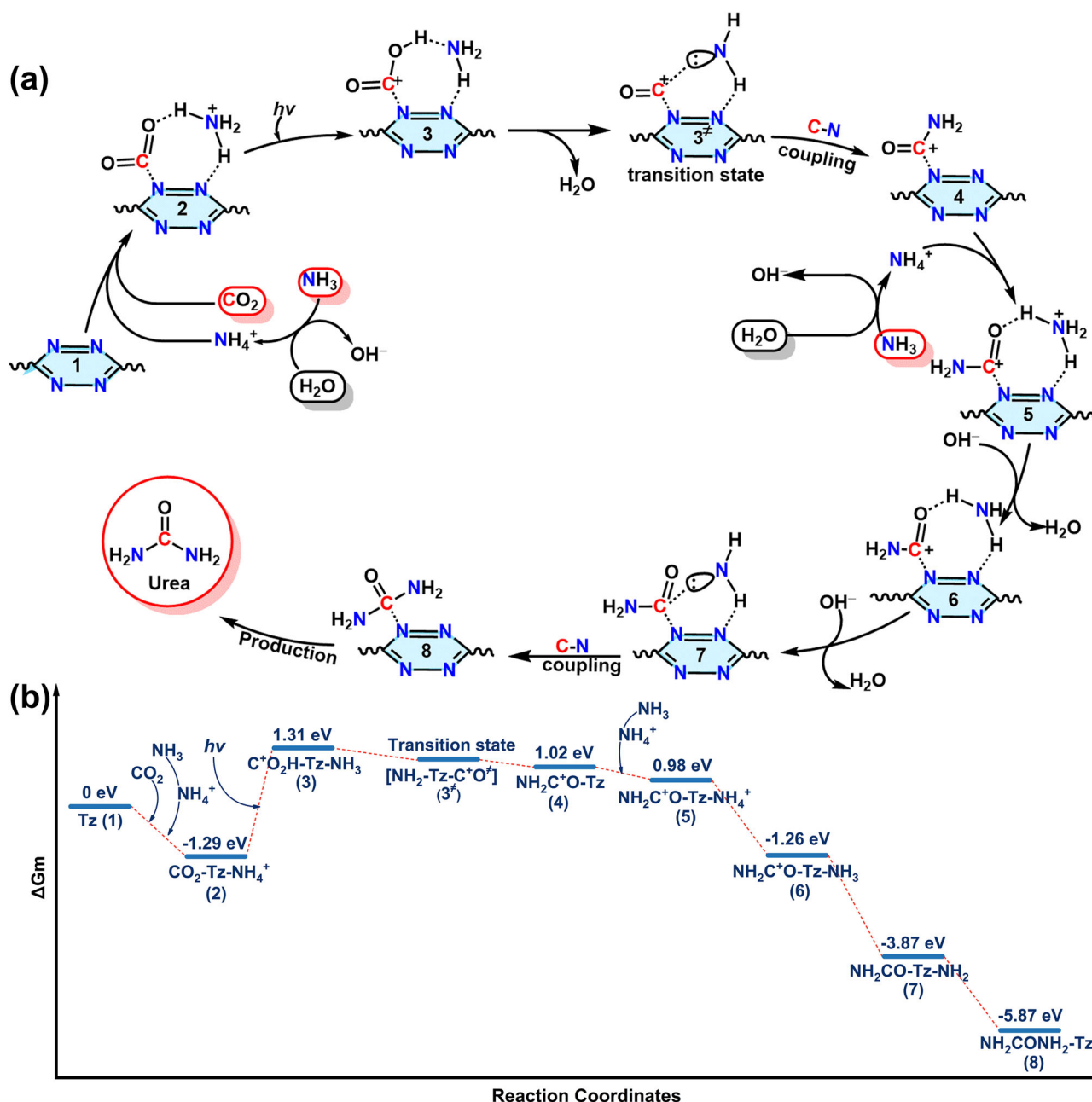
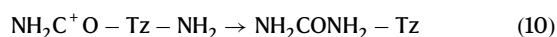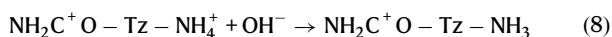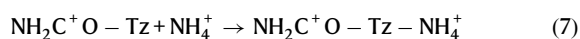$$C^+O - Tz - NH_2 \rightarrow NH_2C^+O - Tz \quad (6)$$

Fig. 4 | DFT calculations. a The reaction pathway and (**b**) corresponding free energy for the generation of urea from CO_2 and NH_3 on 3D-TBBD-COF.

After the construction of NH_2C^+O, one of the two directly connected N absorbing sites in the N = N unit of tetrazine moiety becomes empty again, which would attract a new NH_4^+ ion and form a new co-adsorbing structure of NH_2C^+O-Tz-NH_4^+ according to Eq. (7). Immediately, the dehydration (Eqs. (8) and (9)) and C-N coupling processes (Eq. (10)) are repeated in this stage, leading to the formation of the urea NH_2CONH_2.

$$NH_2C^+O - Tz + NH_4^+ \rightarrow NH_2C^+O - Tz - NH_4^+ \quad (7)$$

$$NH_2C^+O - Tz - NH_4^+ + OH^- \rightarrow NH_2C^+O - Tz - NH_3 \quad (8)$$

$$NH_2C^+O - Tz - NH_3 + OH^- \rightarrow NH_2C^+O - Tz - NH_2 + H_2O \quad (9)$$

$$NH_2C^+O - Tz - NH_2 \rightarrow NH_2CONH_2 - Tz \quad (10)$$

When we look back at the whole catalytic route on 3D-TBBD-COF, it is obvious that all the reactants are crowded together in a very narrow space limited by the two directly connected N atoms with a very short N····N distance of ~1.4 Å in the N = N units of tetrazine moiety, favoring the C-N coupling between $^*C^+O$ and $^*NH_2$ intermediates without energy barrier. This, however, is not the case for 3D-PDDP-COF and 3D-TPT-COF. For 3D-PDDP-COF, the two reactants, CO_2 and NH_4^+, can not depend on the two oppositely arranged N atoms in one pyrazine moiety with N····N distance of ~2.6 Å to proceed with the C-N coupling, Supplementary Figs. 43 and 44. Fortunately, these two reactants are able to depend on two pyrazine N atoms in neighboring layers in the framework with N····N distance of ~3.5 Å to complete the C-N coupling. This, however, requires an obvious energy barrier of 2.00 eV, leading to a significantly weakened photocatalytic CO_2 and NH_3 coupling efficiency, Supplementary Figs. 45 and 46. This is in good agreement with the experimental findings as detailed above. For 3D-TPT-COF,

CO_2 and NH_3 co-adsorption and the following C-N coupling could not be achieved owing to the lack of N adsorption sites in the benzene moiety for CO_2 and NH_4^+. As a total result, the strong spatial confinement effect due to the two directly connected N atoms in the $N=N$ units of tetrazine moiety plays a key role in the C-N coupling process in comparison with 3D-PDDP-COF and 3D-TPT-COF, leading to the efficient urea production with a high rate on 3D-TBBD-COF.

In summary, a series of 3D COFs functionalized with benzene, pyrazine, and tetrazine active cores have been designed and synthesized. The catalytic microenvironment of these COFs can be adjusted by increasing the number of heterocyclic N atoms in the framework, leading to the gradually enhanced light-harvesting capacity, photogenerated carrier separation efficiency, and co-adsorption capacity towards NH_3 and CO_2 in the order of benzene-, pyrazine-, and tetrazine-containing framework. This enables the tetrazine-containing 3D-TBBD-COF to exhibit much superior photocatalytic activity towards urea production from CO_2 and NH_3 to 3D-TPT-COF and 3D-PDDP-COF. In situ DRIFTS investigation and theoretical calculations unveil the C-N coupling reaction between $*C^+O$ and $*NH_2$ intermediates to form crucial intermediate $*NH_2C^+O$ derived from CO_2 reduction and NH_3 oxidation over the $N=N$ centers of tetrazine moiety in 3D-TBBD-COF during the urea formation process. This work lays a way towards sustainable photosynthesis of urea.

Methods

Synthesis of 3D-TBBD-COF
TFPB (15.6 mg, 0.04 mmol) and TBBD (8.8 mg, 0.03 mmol) were weighed into a Pyrex tube with 0.5 mL 1,4-Dioxane and 0.5 mL mesitylene. The mixture was subjected to ultrasonic treatment for 30 minutes to achieve a suspension. Subsequently, 0.2 mL of 6 M acetic acid was added, followed by another 10 minutes of ultrasonic processing. The solution then underwent three freeze-pump-thaw cycles. Thereafter, the Pyrex tubes were hermetically sealed and heated in an oven at 120 °C for 4 days. The precipitate was subsequently isolated via centrifugation and underwent purification through sequential treatments with acetone and tetrahydrofuran for 24 hours. Ultimately, 3D-TBBD-COF was then obtained as a powder with a yield of 65%.

Synthesis of 3D-PDDP-COF
TAPB (14.1 mg, 0.04 mmol) and PDDP (10.4 mg, 0.03 mmol) were weighed into a Pyrex tube with 0.5 mL 1,4-Dioxane and 0.5 mL mesitylene. The mixture was subjected to ultrasonic treatment for 30 minutes to achieve a suspension. Subsequently, 0.2 mL of 6 M acetic acid was added, followed by another 10 minutes of ultrasonic processing. The solution then underwent three freeze-pump-thaw cycles. Thereafter, the Pyrex tubes were hermetically sealed and heated in an oven at 120 °C for 4 days. The precipitate was subsequently isolated via centrifugation and underwent purification through sequential treatments with acetone and tetrahydrofuran over 24 hours. Ultimately, 3D-PDDP-COF was then obtained as a powder with a yield of 60%.

Synthesis of 3D-TPT-COF
TFPB (15.6 mg, 0.04 mmol) and TPT (8.7 mg, 0.03 mmol) were weighed into a Pyrex tube with 0.5 mL 1,4-Dioxane and 0.5 mL mesitylene. The mixture was subjected to ultrasonic treatment for 30 minutes to achieve a suspension. Subsequently, 0.2 mL of 6 M acetic acid was added, followed by another 10 minutes of ultrasonic processing. The solution then underwent three freeze-pump-thaw cycles. Thereafter, the Pyrex tubes were hermetically sealed and heated in an oven at 120 °C for 4 days. The precipitate was subsequently isolated via centrifugation and underwent purification through sequential treatments with acetone and tetrahydrofuran over

24 hours. Ultimately, 3D-TPT-COF was then obtained as a powder with a yield of 80%.

Data availability
All relevant data that support the findings of this study are presented in the manuscript and supplementary information file. Source data are provided with this paper.

References

1. Zhang, X. et al. Managing nitrogen for sustainable development. *Nature* **528**, 51–59 (2015).
2. Erisman, J. W., Sutton, M. A., Galloway, J., Klimont, Z. & Winiwarter, W. How a century of ammonia synthesis changed the world. *Nat. Geosci.* **1**, 636–639 (2008).
3. Qiao, J., Liu, Y., Hong, F. & Zhang, J. A review of catalysts for the electroreduction of carbon dioxide to produce low-carbon fuels. *Chem. Soc. Rev.* **43**, 631–675 (2014).
4. Aresta, M., Dibenedetto, A. & Angelini, A. Catalysis for the valorization of exhaust carbon: from CO_2 to chemicals, materials, and fuels. technological use of CO_2. *Chem. Rev.* **114**, 1709–1742 (2014).
5. Service, R. F. New recipe produces ammonia from air, water, and sunlight. *Science* **345**, 610–610 (2014).
6. Soued, C., Harrison, J. A., Mercier-Blais, S. & Prairie, Y. T. Reservoir CO_2 and CH_4 emissions and their climate impact over the period 1900–2060. *Nat. Geosci.* **15**, 700–705 (2022).
7. Kim, S.-K. et al. Widespread irreversible changes in surface temperature and precipitation in response to CO_2 forcing. *Nat. Clim. Chang.* **12**, 834–840 (2022).
8. Hepburn, C. et al. The technological and economic prospects for CO_2 utilization and removal. *Nature* **575**, 87–97 (2019).
9. von der Assen, N., Jung, J. & Bardow, A. Life-cycle assessment of carbon dioxide capture and utilization: avoiding the pitfalls. *Energy Environ. Sci.* **6**, 2721–2734 (2013).
10. Luo, Y. et al. Selective electrochemical synthesis of urea from nitrate and CO_2 via relay catalysis on hybrid catalysts. *Nat. Catal.* **6**, 939–948 (2023).
11. Hao, Y.-C. et al. Promoting nitrogen electroreduction to ammonia with bismuth nanocrystals and potassium cations in water. *Nat. Catal.* **2**, 448–456 (2019).
12. Liu, J., Guo, X., Frauenheim, T., Gu, Y. & Kou, L. Urea electrosynthesis accelerated by theoretical simulations. *Adv. Funct. Mater.* **34**, 2313420 (2024).
13. Wan, Y., Zheng, M., Yan, W., Zhang, J. & Lv, R. Fundamentals and rational design of heterogeneous C-N coupling electrocatalysts for urea synthesis at ambient conditions. *Adv. Energy Mater.* **14**, 2303588 (2024).
14. Li, D. et al. Accelerating electron-transfer dynamics by TiO_2-immobilized reversible single-atom copper for enhanced artificial photosynthesis of urea. *Adv. Mater.* **34**, 2207793 (2022).
15. Yang, S. et al. Photocatalytic C–N coupling towards urea synthesis with a palladium-supported CeO_2 catalyst. *Catal. Sci. Technol.* **13**, 1855–1865 (2023).
16. Yang, S. et al. Photocatalytic Co-reduction of N_2 and CO_2 with CeO_2 catalyst for urea synthesis. *Angew. Chem. Int. Ed.* **62**, e202312076 (2023).
17. Shi, C. et al. Nitric acid-mediated artificial urea photo-synthesis with N_2 And CO_2. *Adv. Energy Mater.* **14**, 2400201 (2024).
18. Zhang, Y. et al. Synergy of photogenerated electrons and holes toward efficient photocatalytic urea synthesis from CO_2 and N_2. *Angew. Chem. Int. Ed.* **63**, e202405637 (2024).
19. Mao, C., Byun, J., MacLeod, H. W., Maravelias, C. T. & Ozin, G. A. Green urea production for sustainable agriculture. *Joule* **8**, 1224–1238 (2024).
20. Chen, C. et al. Coupling N_2 and CO_2 in H_2O to synthesize urea under ambient conditions. *Nat. Chem.* **12**, 717–724 (2020).

21. Kim, J., Johnson, T. A., Miller, J. E., Stechel, E. B. & Maravelias, C. T. Fuel production from CO_2 using solar-thermal energy: system level analysis. *Energy Environ. Sci.* **5**, 8417–8429 (2012).

22. Hu, W.-Y. et al. Integrating Pd(I) atoms in schottky junctions for visible-light-driven urea production from ambient nitrogenous species and CO_2. *CCS Chem.* **6**, 3008–3017 (2024).

23. Hu, Y. et al. Molecular recognition with resolution below 0.2 angstroms through thermoregulatory oscillations in covalent organic frameworks. *Science* **384**, 1441–1447 (2024).

24. Chang, J.-N. et al. Redox molecular junction metal-covalent organic frameworks for light-assisted CO_2 energy storage. *Angew. Chem. Int. Ed.* **63**, e202402458 (2024).

25. Yang, Y. et al. Electroactive covalent organic framework enabling photostimulus-responsive devices. *J. Am. Chem. Soc.* **144**, 16093–16100 (2022).

26. Wang, X. et al. 12 connecting sites linked three-dimensional covalent organic frameworks with intrinsic non-interpenetrated shp topology for photocatalytic H_2O_2 synthesis. *Angewa. Chem. Int. Ed.* **63**, e202401014 (2024).

27. Gao, Y. et al. Unprecedented POSS-linked 3D covalent organic frameworks with 2-fold interpenetrated scu or sqc topology regulated by porphyrin center for photocatalytic CO_2 reduction. *Angew. Chem. Int. Ed.* **63**, e202404156 (2024).

28. Neumann, S. E. et al. The propensity for covalent organic frameworks to template polymer entanglement. *Science* **383**, 1337–1343 (2024).

29. Yu, B. et al. Construction of single-crystal 3D covalent organic framework with three crossing sets of 2D sheets entanglement. *Chem* **10**, 2170–2179 (2024).

30. Yang, M.-Y. et al. Three-motif molecular junction type covalent organic frameworks for efficient photocatalytic aerobic oxidation. *J. Am. Chem. Soc.* **146**, 3396–3404 (2024).

31. Xu, T. et al. Constructing photocatalytic covalent organic frameworks with aliphatic linkers. *J. Am. Chem. Soc.* **146**, 20107–20115 (2024).

32. Gong, Y.-N., Guan, X. & Jiang, H.-L. Covalent organic frameworks for photocatalysis: synthesis, structural features, fundamentals and performance. *Coord. Chem. Rev.* **475**, 214889 (2023).

33. Tong, L. et al. Atomically precise regulation of the n-heterocyclic microenvironment in triazine covalent organic frameworks for coenzyme photocatalytic regeneration. *J. Am. Chem. Soc.* **146**, 21025–21033 (2024).

34. Liao, Q. et al. Regulating relative nitrogen locations of diazine functionalized covalent organic frameworks for overall H_2O_2 photosynthesis. *Angew. Chem. Int. Ed.* **62**, e202310556 (2023).

35. Lv, S. et al. Metal-coordinated covalent organic frameworks as advanced bifunctional hosts for both sulfur cathodes and lithium anodes in lithium–sulfur batteries. *J. Am. Chem. Soc.* **146**, 9385–9394 (2024).

36. Yu, B. et al. Linkage conversions in single-crystalline covalent organic frameworks. *Nat. Chem.* **16**, 114–121 (2024).

37. Li, N. et al. Hydrophobic trinuclear copper cluster-containing organic framework for synergetic electrocatalytic synthesis of amino acids. *Adv. Mater.* **36**, 2311023 (2024).

38. Kang, X. et al. Reticular synthesis of tbo topology covalent organic frameworks. *J. Am. Chem. Soc.* **142**, 16346–16356 (2020).

39. Zhu, D. et al. Three-dimensional covalent organic frameworks with pto and mhq-z topologies based on Tri- and tetratopic linkers. *Nat. Commun.* **14**, 2865 (2023).

40. Lan, Y. et al. Materials genomics methods for high-throughput construction of COFs and targeted synthesis. *Nat. Commun.* **9**, 5274 (2018).

41. Wu, Y. et al. Nitrogen effects endowed by doping electron-withdrawing nitrogen atoms into polycyclic aromatic hydrocarbon fluorescence emitters. *J. Am. Chem. Soc.* **146**, 15977–15985 (2024).

42. Huang, Y. et al. Direct electrosynthesis of urea from carbon dioxide and nitric oxide. *ACS Energy Lett.* **7**, 284–291 (2022).

43. Hu, Q. et al. Pulsed co-electrolysis of carbon dioxide and nitrate for sustainable urea synthesis. *Nat. Sustain.* **7**, 442–451 (2024).

44. Ou, H. et al. Carbon nitride photocatalysts with integrated oxidation and reduction atomic active centers for improved CO_2 conversion. *Angew. Chem. Int. Ed.* **61**, e202206579 (2022).

45. Liu, P., Zheng, C., Liu, W., Wu, X. & Liu, S. Oxidative redispersion-derived single-site Ru/CeO_2 catalysts with mobile Ru complexes trapped by surface hydroxyls instead of oxygen vacancies. *ACS Catal.* **14**, 6028–6044 (2024).

46. Liu, G., Sun, H., Wang, H. & Qu, Z. Rational tuning towards B-sites (B = Mn, Co, Al) on CoB_2O_4 binary oxide for efficient selective catalytic oxidation of ammonia. *Chem. Eng. J.* **453**, 139941 (2023).

47. Yan, Q., Chen, S., Zhang, C., Wang, Q. & Louis, B. Synthesis and catalytic performance of $Cu_1Mn_{0.5}Ti_{0.5}O_x$ mixed oxide as low-temperature NH_3-SCR catalyst with enhanced SO_2 resistance. *Appl. Catal. B Environ.* **238**, 236–247 (2018).

48. Zheng, S. et al. Multi-center cooperativity enables facile C–C coupling in electrochemical CO_2 reduction on a Ni_2P catalyst. *ACS Catal.* **13**, 2847–2856 (2023).

49. Nan, R., Li, Y., Zhu, Z., Qi, F. & Xiao, X.-Q. Nickelacarborane-supported Bis-N-heterocyclic carbenes. *J. Am. Chem. Soc.* **145**, 15538–15546 (2023).

50. Li, B., Luo, B., Yang, H. & Tang, W. Heck reaction of N-heteroaryl halides for the concise synthesis of chiral α-heteroaryl-substituted Heterocycles. *Angew. Chem. Int. Ed.* **61**, e202209087 (2022).

51. Zhang, X. et al. Electrocatalytic urea synthesis with 63.5 % faradaic efficiency and 100 % N-selectivity via one-step C–N coupling. *Angew. Chem. Int. Ed.* **62**, e202305447 (2023).

Acknowledgements

Author contributions

Conceptualization: J.J., K.W., N.L. Methodology: K.W., N.L. Investigation: N.L., J.Z., X.X. Visualization: K.W., N.L., J.L., Y.L. DFT Calculation: D.Q., N.L. Writing—original draft: J.J., K.W., N.L. Writing—review and editing: J.J., K.W., N.L., D.Q.

Competing interests

The authors declare no competing interests.

Additional information

Supplementary information The online version contains supplementary material available at https://doi.org/10.1038/s41467-025-56307-w.

Correspondence and requests for materials should be addressed to Kang Wang, Dongdong Qi or Jianzhuang Jiang.

Peer review information *Nature Communications* thanks Hai-Long Jiang, Jungang Hou and Rahul Banerjee for their contribution to the peer review of this work. A peer review file is available.

Reprints and permissions information is available at http://www.nature.com/reprints